The effects of energy density and heat treatment on the microstructure and mechanical properties of laser additive manufactured Haynes 282

John Boswell [a], Jonathan Jones [b], Nicholas Barnard [b], Daniel Clark [a], Mark Whittaker [b], Robert Lancaster [b,*]

[a] Rolls-Royce plc., P.O. Box 31, Derby, DE24 8BJ, United Kingdom
[b] Swansea University, Bay Campus, Fabian Way, Swansea SA1 8EN, United Kingdom

ABSTRACT

The nickel-based superalloy Haynes 282 is a promising candidate material among the existing batch of aerospace alloys for manufacture via laser powder bed fusion (LPBF). LPBF Haynes 282 has a strong preference for epitaxial grain growth in the (0 0 1) orientation, promoting inhomogeneous grain morphologies and anisotropic mechanical behaviour. In this paper, LPBF Haynes 282 specimens have been extracted from perpendicular and parallel orientations in respect to the primary vertical build direction and studied in their original as-built form and when exposed to a solution and age heat treatment. The effect of alternative energy densities is also considered in the different conditions. Results show that the numerous processing variables discussed in this research have a direct influence on the morphology of the final grain structure. Although a strongly anisotropic microstructure was present in the as-built material in both respective orientations, this behaviour was eradicated following the solution and aging heat treatment through recrystallisation, and the alleviation of local texture and misorientation to help produce a more uniform equiaxed grain morphology. The subsequent mechanical behaviour has been assessed through hardness, tensile and creep stress rupture testing, and results have corroborated the microstructural findings to confirm a more isotropic material was successfully achieved.

© 2021 The Author(s). Published by Elsevier Ltd. This is an open access article under the CC BY license (http://creativecommons.org/licenses/by/4.0/).

1. Introduction

Additive manufacturing (AM) is a disruptive technology, which enables new design concepts in aerospace propulsion to be realised. Conventional manufacturing technologies, such as investment casting, are limited either by the strength of the removable ceramic cores, which form internal cooling passages, or by the ability to add film cooling holes either using laser drilling or electrical discharge machining (EDM). AM, and more specifically the process of Laser Powder Bed Fusion (LPBF), are of particular interest to design engineers since these technologies allow for the innovation of more complex alloy designs, together with the ability to fabricate highly intricate components [1]. Given the continuously evolving nature of AM components, a detailed understanding of the key process variables and their influence on the final mechanical performance on the component is still yet to be fully understood for exploitation in critical applications [2]. Thomas et al [3] looked to capture the influence of many of these parameters in the normalised process diagram, which helped to illustrate the effects of key process variables, including beam power, energy den-

sity and layer height, on the resulting structures of several alloy systems. Furthermore, since LPBF components typically exhibit features such as epitaxial grain growth promoting textured microstructures parallel to the build direction and in some cases residual stresses due to the high thermal gradients present during the manufacturing process [4,5], a more detailed and holistic understanding is now paramount. A final consideration of the challenges associated with LPBF of nickel-base superalloys are productivity and weldability [6,7]. The requirement to produce parts at the optimum build rates to meet production requirements is offset by the poor weldability of high γ' alloys necessary to meet the demanding high temperature service requirements of modern combustion and turbine components.

Haynes 282 is a γ' strengthened alloy typically used in its wrought or sheet form. The alloy is used in aerospace and land-based gas turbines for static components such as compressor and turbine casings and, due to its good weldability [8], has also found application in fabricated components such as exhaust nozzles or diffusers. In the wrought condition, Haynes 282 is known to offer a favourable balance of mechanical properties and fabricability, superior to other prominent Ni based alloy systems such as Waspaloy. The mechanical behaviour is largely dictated by the low volume fraction of γ' precipitates in a microstructure which also

---

* Corresponding author.
    E-mail address: r.j.lancaster@swansea.ac.uk (R. Lancaster).

typically comprises of MC, M_6C and $M_{23}C_6$ carbides which also contribute to the material's strength. The nominal composition of the alloy is presented in Table 1.

In the LPBF form, Haynes 282 is found to offer comparable mechanical properties to the wrought material, given the weldability of the alloy which is often regarded as a tangible indicator of whether the material is suitable for LPBF manufacture. Shaikh et al [9] found that the as-built LPBF material exhibited a columnar grain structure, as typical of the LPBF process, but with a finer grain size (<30 μm) as compared to wrought (65–90 μm). However, after a suitable heat treatment, the microstructure was revealed to contain γ, γ′ and carbide phases, similar to those that are seen in the wrought material, but with a change in morphology. In the wrought material, there was a continuous carbide morphology along the grain boundaries, whereas in the LPBF variant, there was a finer, discrete dispersion of carbides found at grain boundary locations. This led to a change in the stress rupture performance at a temperature of 927 °C, as the LPBF vertically built Haynes 282 material offered superior creep rupture properties (time to rupture of 146.7 ± 15.6 h) compared to the plate equivalent (100 h) [9].

Whereas such studies have shown that post-processing treatments can be applied to alleviate some of the material's underlying anisotropy and inherent residual stresses to improve propeties, typically through optimised heat treatments [10], there is still a lack of knowledge as to how an alloy can be treated to become more weldable whilst maintaining its fundamental strength properties. This study will examine the effects of energy density, sample geometry and post build solution heat treatment on the as-built microstructure of LPBF Haynes 282. Hardness, tensile and stress rupture tests have been carried out to assess the effects of build parameters on post heat treatment mechanical properties. Experimental findings are supported by comprehensive microstructural investigations including primary dendrite arm spacing (PDAS) measurements and electron backscatter diffraction (EBSD) studies to capture and quantify the microstructural changes observed in the material in the different conditions.

2. Materials and methods

2.1. Material

Gas atomised Haynes 282 powder was supplied by Praxair and characterisation was carried out at the Manufacturing Technology Centre (MTC) in Coventry. The measured particle size distribution (D_{10} = 13.6 μm, D_{50} = 25.1 μm and D_{90} = 44.1 μm) is within specification although the low D_{10} value represents a relatively larger distribution of finer sub-30 μm particles. Carr's index and Hausner ratio of 1.17 and 14.86 are within the range specified for good, free flowing powder. Inductively coupled plasma mass spectrometry (ICP-MS) indicated a slight deficiency in Boron content, as given in the powder chemistry detailed in Table 2.

2.2. LPBF build

The LPBF samples were built using an EOS M290 laser 3D printing system, fitted with a 400 W ytterbium fibre laser. Parameters were defined using a design of experiments (DoE) methodology [11] which was part of a previous study. Three sets of optimised

parameters were developed for a 30 μm layer thickness. The actual parameters used in the study are Rolls-Royce plc. proprietary data and have, therefore, been omitted. The parameters are subsequently described as, low, medium and high, representing the relative energy densities for the different parameters, as detailed in Table 3.

The number of parameters was reduced further based on specific energy limits, as specified in Eq. (1), where energy density (ED is calculated by:

$$ED = 1.5 < \frac{P}{(h.v)} < 3.5 \qquad (1)$$

Where P represents power (W), h is hatch distance (mm) and v is line speed (mm/s).

The sample geometry used in the study is based on the work carried out by Risse [12] as part of the EU funded MERLIN research programme and is illustrated in Fig. 1. Please note that the simulated cooling holes are for a related study.

2.3. Heat treatment

The heat treatments adopted in this research differ from the conventional heat treatments used for wrought Haynes 282. Previous studies [13,14] showed that supersolvus γ′ heat treatments are required to reform the as-built microstructure through grain recrystallisation in LPBF CM247LC. Similarly, solution heat treatments on LPBF Haynes 282 require higher temperatures to ensure that recrystallisation takes place. For example, typical solution heat treatment temperatures for wrought materials are 1150 °C [15], whereas the solution heat treatment temperature used in some experiments is 1250 °C. The heat treatment schedule used in these experiments is detailed in Table 4, which consists of a single age heat treatment at 788 °C following a solution heat treatment for 1 h at 1250 °C.

2.4. Microstructural analysis

2.4.1. Porosity and Micro-cracking

For visual analysis, specimens were mounted in conductive Bakelite, ground using silicon carbide papers between 200 and 4000 grit, then polished using diamond media between 9 μm and 1 μm. A final polish was carried out using OPS colloidal silica. A series of 3 × 3 mm mosaic micrographs were taken for 3 separate areas with a magnification of x100 to assess cracking and porosity in the as-built and heat treated condition. Measurements were carried out in both the Y-Z plane (parallel to the build direction) and the X-Y plane (perpendicular to the build direction). Crack density measurements were recorded using the crack length measurements obtained from ImageJ™ software.

2.4.2. Grain size

In accordance with ASTM E112-13 [16], grain size measurements were recorded in both the as-built and heat treated conditions. Samples were polished using OP-S colloidal silica for 5 min to reveal the grain boundaries and x100 BSE SEM micrographs captured both the Y-Z and X-Y planes. Measurement was carried out using ImageJ™ software.

Table 1
Nominal composition of Haynes 282 Alloy (wt%).

Ni	Cr	Co	Mo	Ti	Al	Fe	Mn	Si	C	B
57 (Bal)	20	10	8.5	2.1	1.5	1.5 (Max)	0.3 (Max)	0.15 (Max)	0.06	0.05

Table 2

Haynes 282 powder chemistry (wt%).

	Cr	Al	Ti	Mo	Sn	B	P	O	N	H
Specification	18.9–19.9	1.50–1.65	2.0–2.2	8.3–8.8	<0.005	0.003–0.005	<0.010	–	–	_
Mean	19.54	1.56	2.12	8.57	0.0006	0.0027	0.0015	0.014	0.0067	0.0007
Relative Standard Deviation (+/- %)	1.09	1.03	1.04	1.18	21.8	2.5	40.8	9.29	2.63	0.076

Table 3

Experimental build parameters.

Designation	Energy Density / J/mm^2
Low	1.60
Medium	2.29
High	3.20
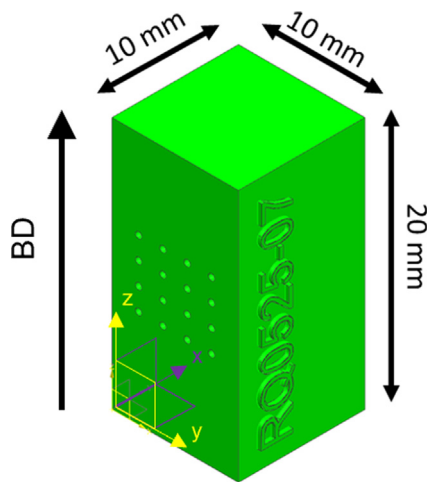
Fig. 1. Sample geometry for vertically built LPBF samples.

Fig. 2. Primary dendrite arm spacing (PDAS) morphology.

2.4.3. Primary dendrite arm spacing

Primary dendrite arm spacing (PDAS) measurements were carried out on electrolytically etched samples. The specimens were etched in 10% phosphoric acid solution, with 4 V for 30 s. Samples were examined using a Phillips XL30, field emission gun (FEG) scanning electron microscope (SEM). A series of x5k magnification images of the as-built microstructure were used to measure the PDAS using a mean linear intercept (MLI) method based on the grain size assessment method defined in ASTM E112-13 [16]. Only measurements perpendicular to the dendrite growth direction were taken from the images showing the microstructure parallel to the build direction, as depicted in Fig. 2. The mean PDAS is taken as the length (L) divided by the number of cells, or dendrite boundaries intercepting the line. Ten measurements were taken from four separate regions of each sample and the value of PDAS stated is the average of all measurements.

2.4.4. γ' size, shape and volume fraction

The size and volume fraction of the γ' phase was measured in the post heat treated condition. Due to the very fine γ' size
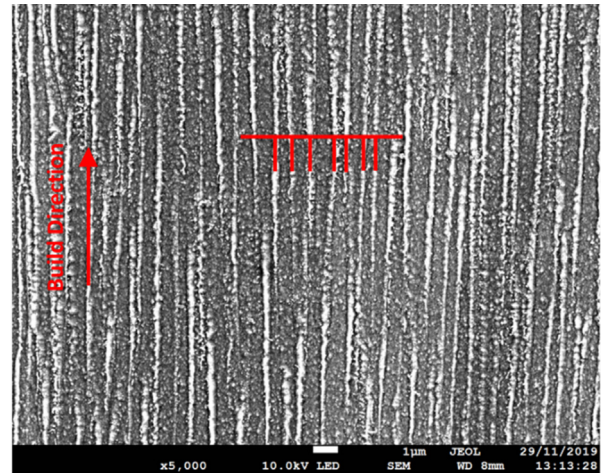
observed, a magnification of x20k was required to clearly define the γ' phase precipitates. Assessment of the γ' phase was carried out using ImageJ™ software; size, area and circularity were measured.

Electron Backscatter Diffraction (EBSD)

Large scale optical micrographs were captured for each variant and selected areas were scanned using electron backscatter diffraction (EBSD), conducted on a Hitachi SU3500 scanning electron microscope (SEM) operated at 20 kV and 100 μA. Data for texture, local misorientation and random grain boundary network analyses were collected through EBSD, where a step size of 0.25 μm was used alongside HKL Channel 50′s elliptical fit method. Misorientation data was analysed using a 7 × 7 neighbourhood and a threshold value of 1°. All EBSD scans performed were taken from the closest position available to the centre of the block section, remote from any simulated cooling holes present.

2.5. Mechanical testing

2.5.1. Micro-hardness HV(1)

Micro-hardness values were recorded on the as-built and post solution heat treated samples using a Vickers hardness indenter. A 1 kg load, HV (1), was used throughout. 25 measurements were taken from each material, across the full width of the sample, and data from the tests was analysed using Minitab statistical analysis software.

Table 4

Heat treatment schedule for Haynes 282.

Heat Treatment	Heating Rate	Soak Temperature / °C	Soak Time / h	Cooling Rate / °C.min^{-1}
Solution	10 °C.min^{-1}	1250	1	*10
Age	No requirement	788	8	Gas Fan Quench

* Note: − 10 °C.min^{-1} represents the target cooling rate for LPBF Haynes 282, acceptable cooling rates are within the range of 5 °C.min^{-1} to 15 °C.min^{-1}.

2.5.2. Tensile testing

Ten tensile tests were performed on round cylindrical specimens (as depicted in Fig. 3) of the post solution heat treated material, using the 'low' parameter set (energy density of 1.60 J/mm^2). All testing was undertaken in accordance with ASTM E21-17 [17] at a temperature of 850 °C. A decision was made to test only the low energy density parameter set since this batch of specimens would be expected to contain the highest levels of porosity, and therefore test results are likely to contain more scatter, specifically for properties such as ultimate tensile strength (σ_{UTS}) and percentage elongation.

2.5.3. Creep stress rupture testing

A series of ten stress rupture creep tests were carried out on specimens of the dimensions depicted in Fig. 4. Similar to the tensile tests, only post solution heat treated specimens with the 'low' parameter set were built. All stress rupture tests were performed in accordance with ASTM E139-11 [18] at a constant test temperature of 750 °C and constant stress of 410 MPa to replicate the conditions that the material would experience in-service.

2.5.4. Statistical analysis

The grain size analysis of variance (ANOVA) method was used to determine the statistical significance of the variance in grain size using a 95% confidence interval. The results are based on combined measurements taken from both the X-Y and Y-Z planes of reference. The factor levels are low, medium and high, referring to the three alternating energy densities and the response for each is derived in terms of mean grain size. The significance level is determined by Eq. (2), and the calculated value is compared to a tabulated reference value for the defined significance level [19]. If the calculated value is greater than the tabulated value based on the number of factors and the sample size, then the Null Hypothesis (H_0), where all means are equal, can be rejected.

$$F = \frac{\left(\frac{n\sum_{i=1}^{a}\left(\bar{y}_{i.}-\right)^2}{(a+1)}\right)}{\left(\frac{\sum_{i=1}^{a}\sum_{j=1}^{n}\left(y_{ij}-\bar{y}_{i.}\right)^2}{a(n-1)}\right)} \tag{2}$$

Where n represents the number of repeats per factor level, a is the number of factor levels (0.05), $\bar{y}_{i.}$ is the average response per level and $\bar{y}_{ij}$ is the average of all responses.

For mechanical properties, an equivalency test has been carried out using the 'Student T-test'. The T statistic has been calculated for tensile and stress rupture properties, as defined in Equation (3),

and the value has been compared to tabulated T distribution values to determine the level of significance of the test. For all the statistical methods, a 95% confidence interval was used. The student T-test is used when the population standard deviation is not known [19].

$$T = \frac{\bar{X}-\mu}{\frac{S}{\sqrt{n}}} \tag{3}$$

Where n represents the number of samples tested, S is the sample standard deviation, $\bar{X}$ is the sample mean for a comparative data set and μ is the population or baseline data set mean. In this research, the baseline data set is represented by the Y-Z plane and the comparison dataset is for samples on the X-Y plane.

3. Results and discussion

3.1. Structural integrity

As discussed previously, Haynes 282 is a weldable nickel-based superalloy [20], therefore very few cracks are expected to be observed in any of the samples examined. As previously reported by Osoba [8] the susceptibility of solidification cracking in wrought Haynes 282 is considerably lower than that observed in similar Ni based superalloys such as In718. Furthermore, the levels of strain age cracking of Haynes 282 have also been previously examined and the authors found little evidence of such cracking due to the slow precipitation of γ' [21]. This is supported by the findings illustrated in Table 5, which displays the crack measurements for samples taken from each of the three density sets. As can be seen, there is limited evidence of cracking in each of the specimens, providing confidence in the build integrity. However, the medium energy density build appears to have fewer cracks, suggesting that this parameter set is likely to be close to the optimum condition for this alloy. A previous study [22] has detailed the influence of solidification and hot cracking on the mechanical behaviour of an alloy of high crack susceptibility, Hastelloy X, as manufactured by LPBF. The authors found after the crack density was reduced by 65%, at an elevated temperature of 1033 K both yield strength and UTS properties were seen to increase.

Porosity measurements are summarised in Table 6 and Fig. 5. It can be seen from the results that the lowest levels of porosity are associated with the high energy density build. However, it should be stated that porosity levels for both high and medium energy densities are essentially the same, as can be observed from the box plot in Fig. 5. Previous studies [11,22] have shown that mini-
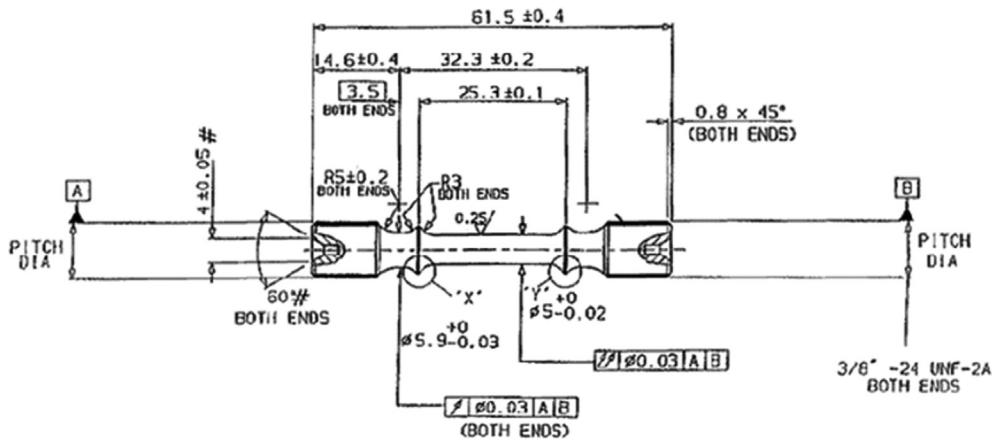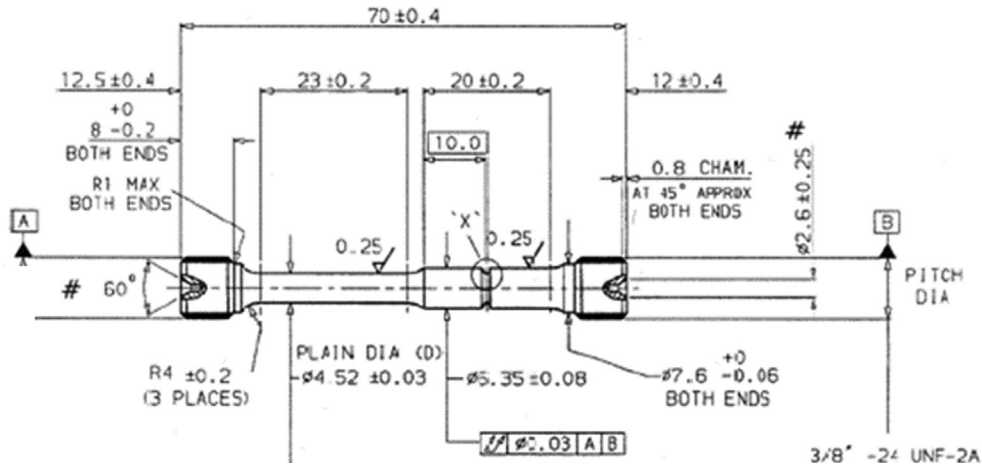

Fig. 3. Tensile test specimen geometry.

Fig. 4. Stress rupture creep test specimen.

Table 5
Summary of observed cracks in Haynes 282 LPBF samples.

Parameter Set	Number of Cracks	Average Crack Length (μm)	Median Crack Length (μm)	Total Crack Length (μm)
Low	5	22	20	112
Medium	1	47	n.a.	47
High	2	55	n.a.	109

Table 6
Summary of porosity measurement results from Haynes 282 LPBF builds.

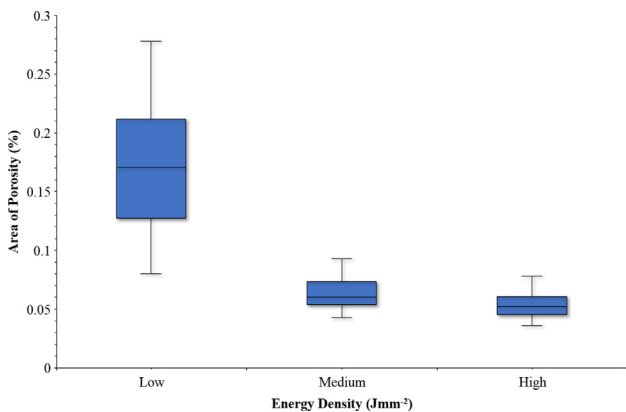| Parameter Set	Mean Area (%)	Standard Deviation	Minimum Area (%)	Maximum Area (%)
Low	0.17	0.06	0.08	0.03
Medium	0.06	0.01	0.04	0.09
High	0.05	0.01	0.04	0.08

Fig. 5. Box plot showing cumulative frequency distributions of porosity measurements for the three parameter sets used in the LPBF build experiments.

mum porosity levels reach a threshold level once the optimum energy density has been achieved and will increase with higher energy densities due to the onset of key-holing [23].

3.2. Grain size

3.2.1. As-built material

Typical as-built AM microstructures are characterised by directionally solidified elongated grains strongly aligned parallel to the build direction (Y-Z plane), as shown in Fig. 6. On the X-Y plane, which is situated perpendicular to the build direction, the

microstructure is typically characterised by fine equiaxed grains, which are the cross-sections of the directionally solidified (DS) columnar grains on the Y-Z plane [24]. Both the shape and crystallographic texture are aligned with the primary heat flux direction, which is due to conduction through the part into the large baseplate that acts as a heat sink [14]. The powder effectively acts as an insulator and prevents lateral heat flow from the part during processing. The effects of convection due to gas flow are also negligible, however the heat flux and hence grain growth direction can be influenced by the scan strategy [25].

For the three parameter sets used in this study, analysis of measured grain size data, as given in Table 7 and Fig. 7, shows that a trend exists where larger average grain sizes can be directly associated with higher line speeds in the Y-Z plane for 30 μm layer thickness builds. Since both power and scan spacing remain constant, the reduction in line speed is effectively an increase in energy density. In the X-Y plane, perpendicular to the vertical build direction, there is an inverse effect of line speed compared to the Y-Z plane (or the vertical build direction); hence higher energy densities result in a larger average grain size. As a result, grains become shorter in height yet wider with increasing energy density, which suggests that both cooling rates and weld pool shapes are modified by line speeds, which in turn affects grain size and shape, as shown in Fig. 7.

3.2.2. Post heat treated material

The post heat treatment grain size measurements for LPBF Haynes 282 are presented in Table 8, displaying the mean, maximum and minimum grain size figures based on measurements from a
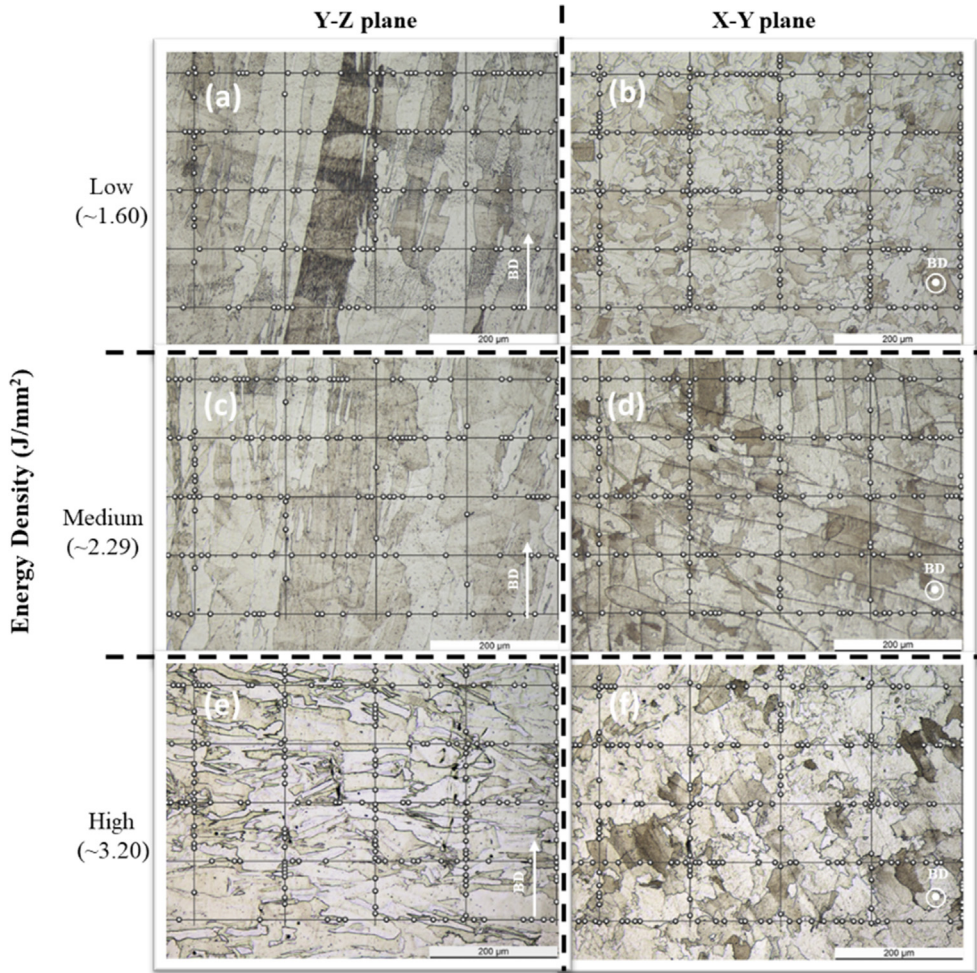
Fig. 6. As-built LPBF Haynes 282 grain structures parallel (Y-Z plane) and perpendicular (X-Y plane) to the vertical build direction for (a) and (b) low energy density melt parameters, (c) and (d) medium energy density, (e) and (f) high energy density (BD refers to build direction).

Table 7
Grain size measurement data from as-built LPBF Haynes 282 microstructures in the X-Y Plane.

Energy Density	As-Built Grain Size Diameter					
	Mean (μm)		Maximum (μm)		Minimum (μm)	
	X-Y	Y-Z	X-Y	Y-Z	X-Y	Y-Z
Low	20.6	31.7	88.5	235.9	0.5	5.2
Medium	24.5	30.4	86.6	166.2	1.7	4.5
High	24.6	24.4	103.9	127.2	5.5	5.5

minimum of 14 locations. It is evident that when comparing the results from the as-built and post heat treatment conditions, as presented in Fig. 8, the melt parameters adopted during the build determine the post heat treatment grain size, and therefore by inference, the post heat treatment mechanical properties.

As shown in Fig. 9, the post heat treatment grain structure has recrystallised and it is difficult to distinguish between the parallel Y-Z plane and the perpendicular X-Y plane, giving an indication of the isotropy now present in the material. The grain structure is bimodal in nature and presents large > 350 μm diameter grains interspersed with much smaller equiaxed grains, <5 μm diameter (Table 8). The variation in grain size due to differences in energy density remains after heat treatment, with higher energy density builds having a larger average grain size than the low energy density builds.

3.3. Primary dendrite arm spacing (PDAS)

3.3.1. As-built material

PDAS measurements were recorded in the as-built condition in both the parallel (Y-Z plane) and perpendicular (X-Y plane) orientations to the vertical build direction, spanning the low to high energy density melt parameter sets defined in Table 3. Initial findings suggest that the mean PDAS increases concurrently with energy density in both orientations (Fig. 10(a)), however a difference in response between the two orientations is apparent. At low energy densities, the mean PDAS measurement calculated in both orientations is very similar at approximately 0.45 μm. However, in the X-Y plane, the mean PDAS increases gradually in a linear manner with energy density, becoming larger than the equivalent PDAS value in the Y-Z plane across the medium energy
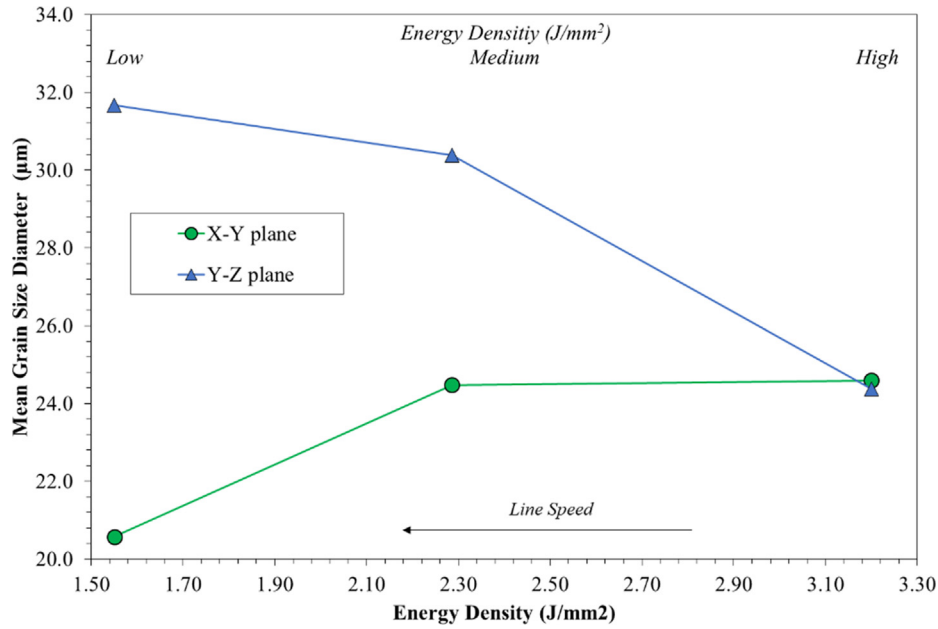
Fig. 7. Mean grain size vs energy density perpendicular to the build direction (X-Y plane), and parallel to the build direction (Y-Z plane) for as-built LPBF Haynes 282.

Table 8
Grain size measurement data from post heat treatment Haynes 282 in the X-Y plane.

Energy Density	Post Heat Treatment Grain Size Diameter		
	Mean (μm)	Maximum (μm)	Minimum (μm)
Low	44	384	2.7
Medium	60	563	2.0
High	69	423	1.6

density levels. Whilst in the Y-Z plane, the mean PDAS increases exponentially once the energy density is greater than around 2.75 J/mm^2, becoming larger than the X-Y plane at high energy densities.

An example of the normal distribution of the PDAS in both the parallel and perpendicular orientations to the vertical build direction under the low energy density build parameters is given in Fig. 10(b). The PDAS in both planes is very similar, albeit slightly larger in the Y-Z plane. This trend is consistent with what would be expected when comparing the as-built mean grain size, in these orientations (Table 7), with the PDAS measurements. In a similar manner to PDAS, the mean grain size is slightly larger in the Y-Z plane than the X-Y plane.

Despite the upmost diligence when acquiring the PDAS measurements, a level of caution is still required when analysing the results. Measurements could have been influenced by the inherent inaccuracies of the MLI measurement technique used. For example,
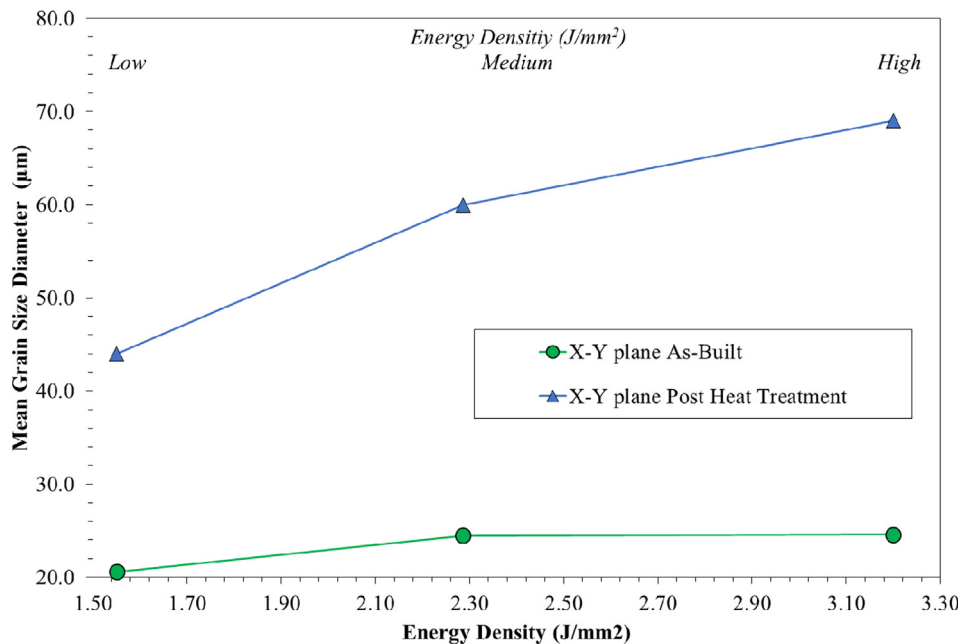

Fig. 8. Mean grain size vs energy density on the perpendicular (X-Y) plane to the vertical build direction for as-received and post heat treated LPBF Haynes 282.
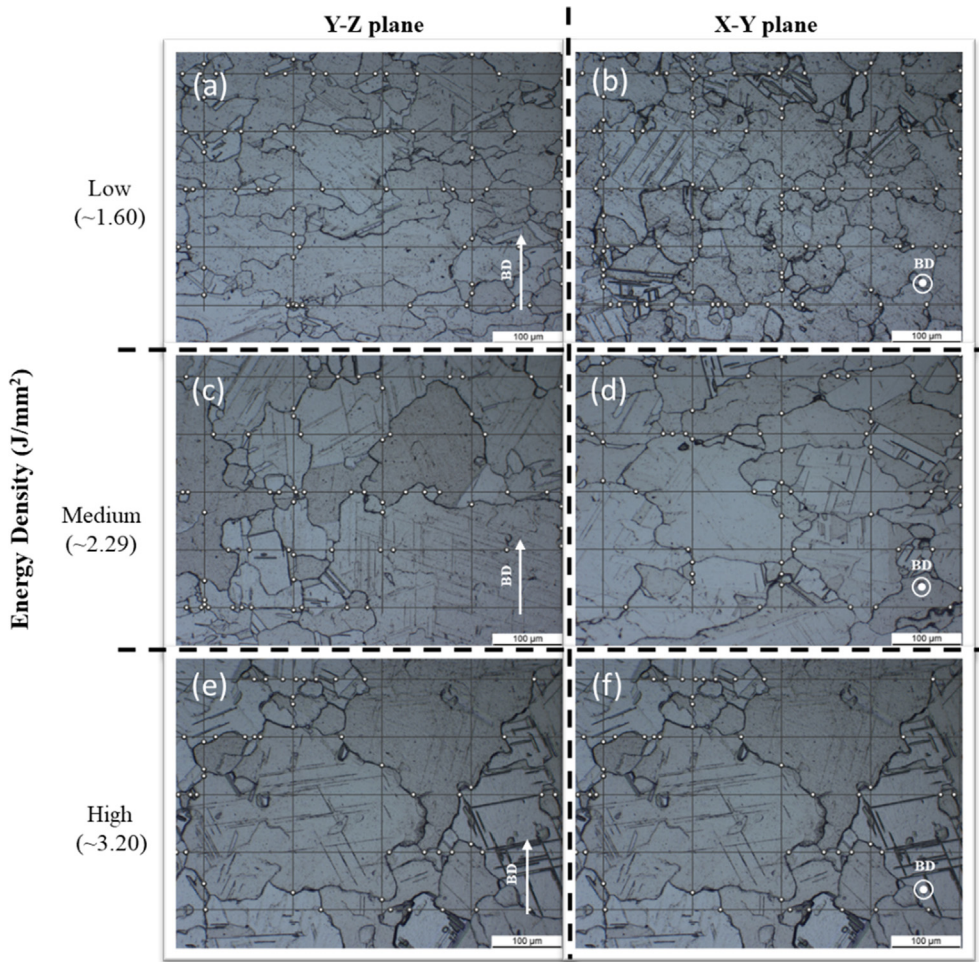
Fig. 9. Post solution and aged LPBF Haynes 282 grain structures parallel (Y-Z plane) and perpendicular (X-Y plane) to the vertical build direction **(a)** and **(b)** low energy density **(c)** and **(d)** medium energy density **(e)** and **(f)** high energy density.
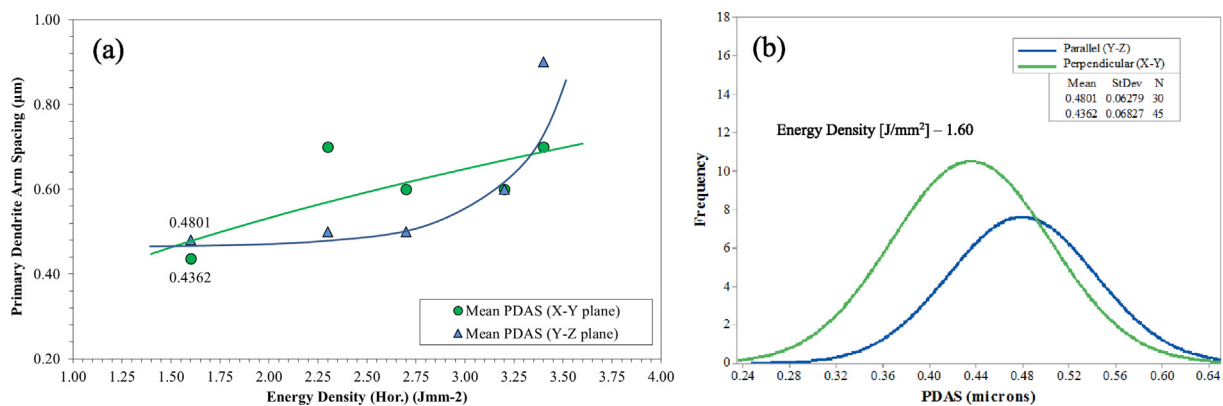

Fig. 10. PDAS measurements taken in the as-built condition on both the parallel (Y-Z), and perpendicular (X-Y) planes to the vertical build direction **a**) Mean PDAS versus energy density **b**) PDAS normal distributions for the low energy density parameter set (~1.60 J/mm^2).

when measuring the orientations perpendicular to the build direction (X-Y plane), errors can be caused by a variation in the angle of the plane intersecting the dendrites. Therefore an oblique plane intersecting the vertically aligned cells or dendrites will result in variations in the spacing measured and since only small differences (100 nm – 200 nm) are being measured, this leads to large amounts of scatter in the data. As such, to acquire a more conclusive picture

of dendritic behaviour, a much larger data set spanning multiple specimens is recommended.

Previous work carried out by Royer [26] showed a relationship between cooling rate and PDAS in LPBF nickel-based alloys. They found that changes in energy density affects melt pool size during deposition and in turn affects the cooling rates during solidification. Due to the high cooling rates associated with LPBF a very fine

cellular dendritic microstructure is produced. Furthermore, relatively large changes in cooling rate, i.e. by up to an order of magnitude, would result in small changes in PDAS. As such, a more accurate method of measurement is required to capture the changes associated with increasing or decreasing energy density, which have been shown to be difficult to distinguish.

The effect of the LPBF process itself and the subsequent solution heat treatment on the dendritic structure was investigated by visually comparing planes parallel (Y-Z) and perpendicular (X-Y) to the vertical build orientation, in both the as-built and post heat treatment conditions under low energy density build parameters. Micrographs of the low energy density, as-built dendritic morphologies in both parallel (Y-Z) and perpendicular (X-Y) orientations are shown at increasing magnification in Fig. 11. For comparative purposes, the orientation and specimen in Fig. 11 (a) and (b), is directly related to those previously presented in Fig. 6 (a) and (b).

The typical layer-by-layer deposition pattern indicating the dendritic/cellular segregation is apparent throughout the structure in both orientations as a result of the programmed AM tooling path. In Fig. 11, repetitive curved bands, which occur within each

build layer, are highlighted in red, and build layer lines are highlighted in dashed white lines. These repetitive bands represent the fusion boundaries between two adjacent laser pulses, with each pulse depositing approximately 10 to 30 μm layers. Whereas the build layer bands, represent a single deposition pass of the laser, depositing approximately a 30 μm layer thickness, previously defined using the three sets of optimised LBPF parameters.

This dendritic morphology is a direct result of the rapid cooling rates during the LPBF process, where denser elements are diffused from the melt pool during the solidification process to the inter-dendritic regions in the microstructure [26]. In the parallel (Y-Z) plane, the dendritic structure is aligned and elongated with the build orientation and thus, the primary heat flux direction. The dendritic growth is in strong cohesion with the directionally solidified (DS) grain growth directions, prevailing at 90° and 66° to the vertical build direction. In the perpendicular (X-Y) plane, cross-sections of the DS columnar grains on the Y-Z plane are visible. As given in Fig. 11(f), boundaries are approximately spaced every 30 μm, consistent with the previously determined particle size distribution Across the fusion / melt pool boundaries, differences in the orientation of the dendritic structure are apparent.
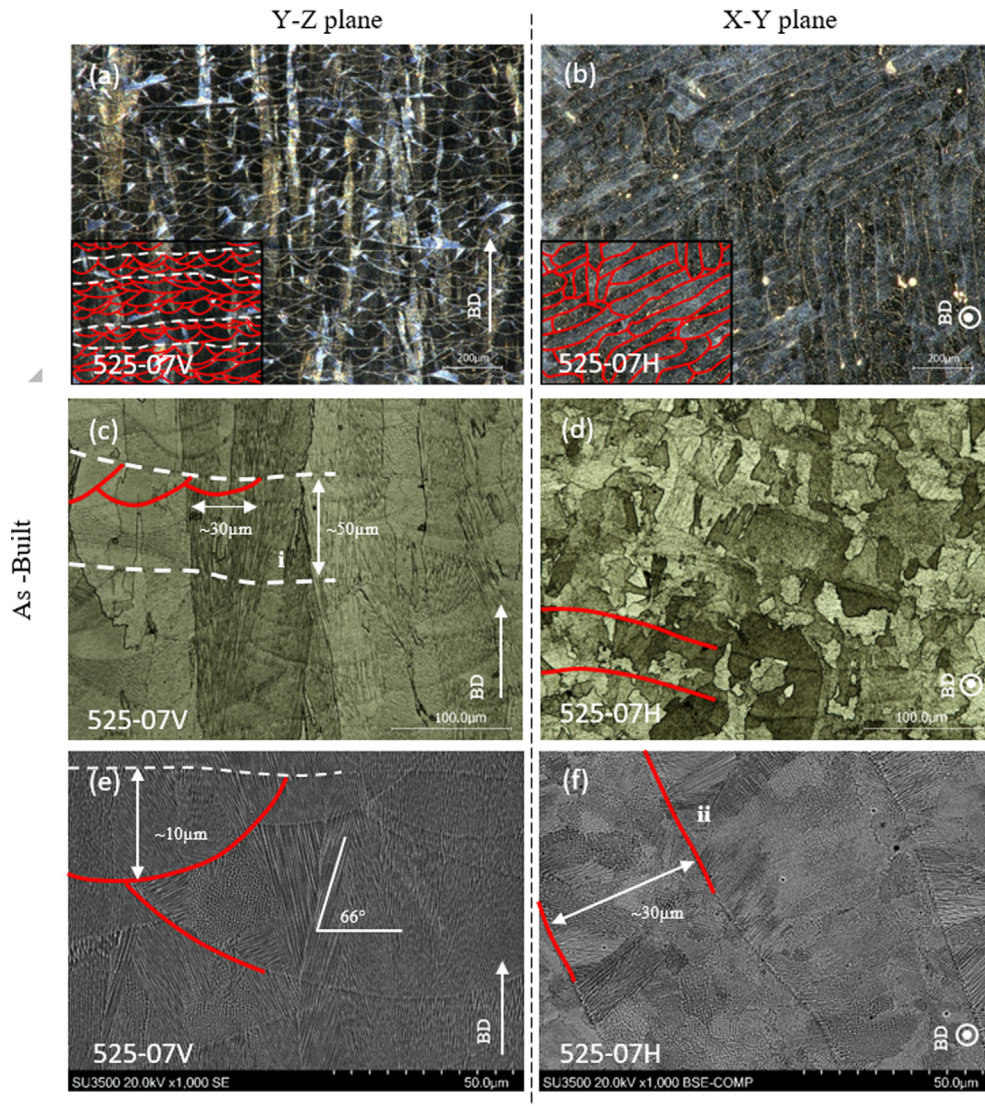

Fig. 11. Micrographs of low energy density build grain morphologies in the as-built condition (a), (c) and (e), Parallel (Y-Z plane) and (b), (d) and (f) Perpendicular (X-Y plane) to the vertical build direction. *i* indicates a build layer fusion line and *ii* represents a discrete build segregation line.

3.3.2. Post heat treatment

In the post heat treatment condition, no dendritic structure was observed. Therefore, no measurement of the PDAS was possible. The recrystallisation and resultant equiaxed microstructural transformations during the heat treatment process could explain the resolution of any dendritic structure. No evidence of the melt pool defects/lines/boundaries can be seen and also appear to have been completely eradicated in orientations both parallel and perpendicular to the vertical build directions, leaving an equiaxed structure as shown in Fig. 12.

3.4. γ' size and volume fraction

The size and volume fraction of γ' precipitates were measured for the low and high energy density samples to determine the likely extremes of the LPBF melt process. The SEM images presented in Fig. 13 show the γ' and carbide morphologies for the two extreme energy density variants, both of which were subjected to the same post build solution heat treatment. Both samples show that γ' is dendritic in form and has the appearance of

being overaged [27]. The sample from the low energy density conditions shows a bi-modal γ' microstructure with both coarse, dendritic and fine secondary γ' concentrated at the grain boundaries. It can also be observed that the carbides along the grain boundaries in the low energy density material appear to be coarser than those found in the higher energy density equivalent, acting to pin the grain boundaries and restrict unwanted grain growth. As reported by Osoba et al [28], a fine grain structure in LPBF Haynes 282 is beneficial for weldability and in this research, is desired for the intended application of the material. Further investigation of the temperature trace from the post build solution heat treatment showed that the cooling rate is approximately 4 °C.min^{-1} (Fig. 14). An optimised heat treatment cycle would result in a finer, more spheroidal γ' phase with a larger volume fraction than the sub-optimum heat treatment used in the experiment [15].

3.5. Electron Back-Scatter diffraction (EBSD)

EBSD scans, which were run over a reduced area compared with those shown in Figs. 6 and 9, can be seen in Fig. 15, in both the par-
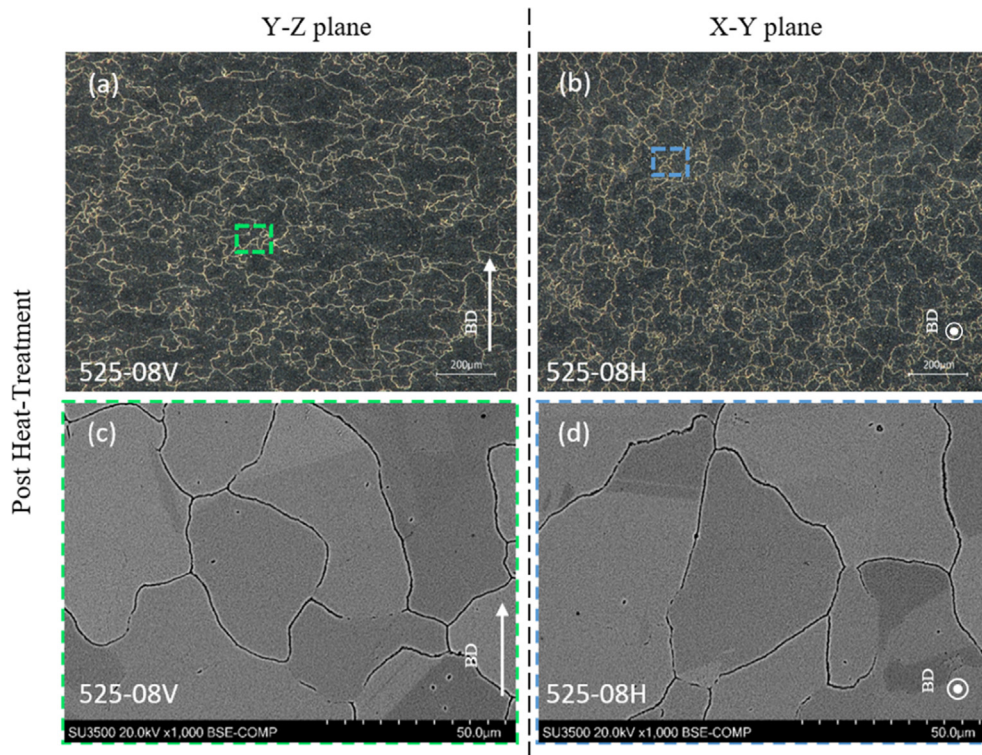

Fig. 12. Grain morphologies of the low energy density build in the post heat treatment condition **(a)** and **(b)** Parallel (Y-Z plane) and **(c)** and **(d)** Perpendicular (X-Y plane) to the vertical build direction.
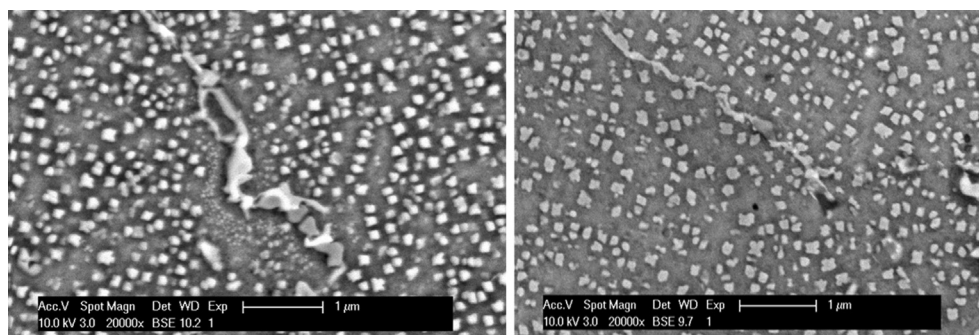

Fig. 13. SEM images of the γ' morphology for **(a)** Low energy density and, **(b)** High energy density conditions.
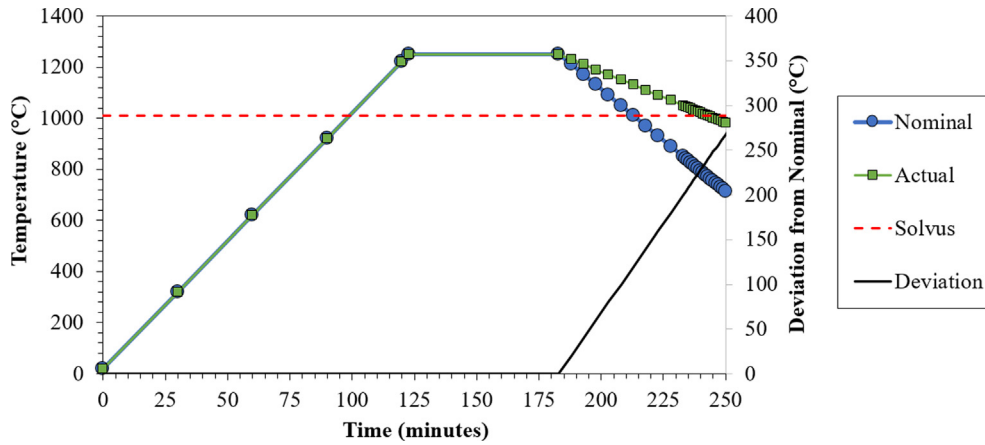
Fig. 14. Furnace temperature trace for solution heat treatment showing the low cooling rate from the solution temperature at 1250 °C.
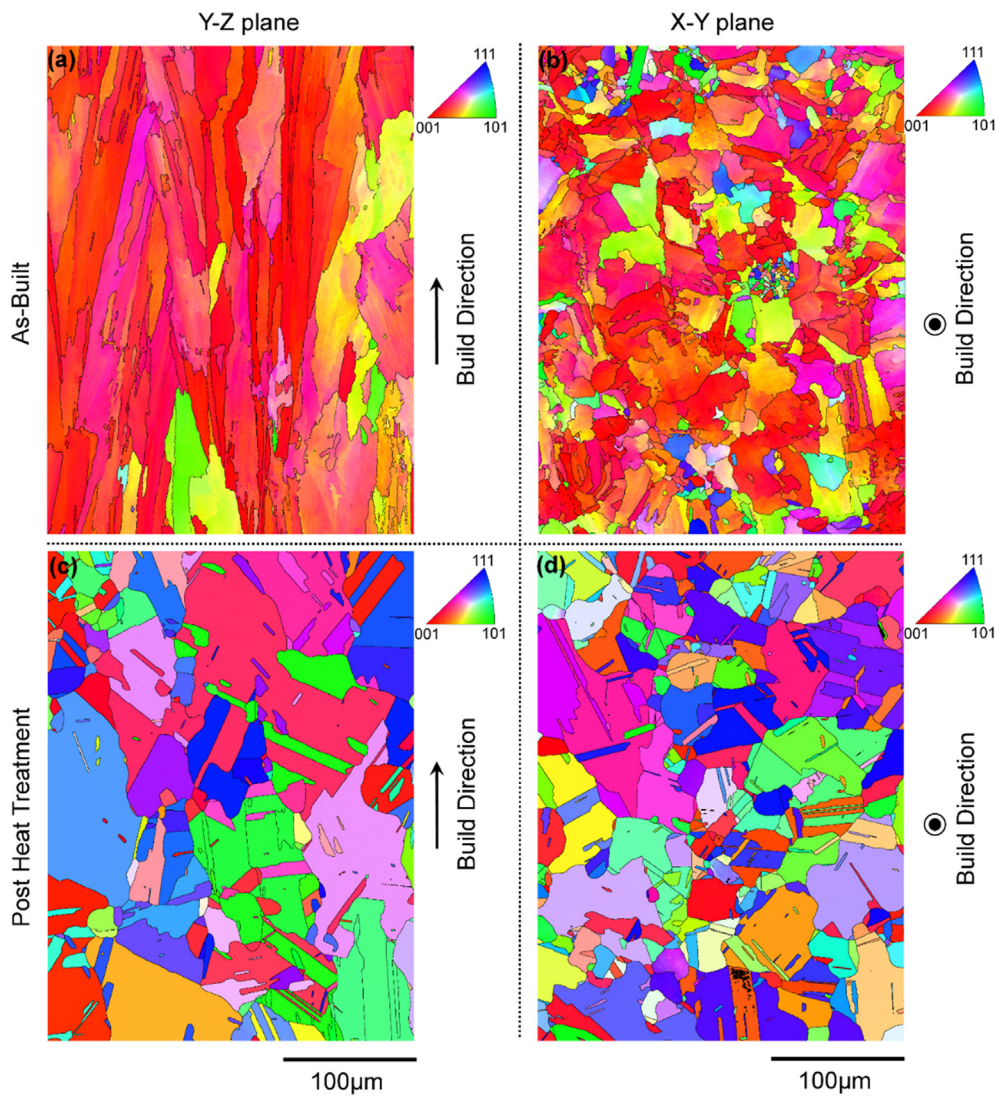

Fig. 15. Inverse pole figure plots from EBSD of the LPBF Haynes 282 material; **(a)** Parallel (Y-Z), and **(b)** Perpendicular (X-Y) planes in the as-built condition and **(c)** Parallel (Y-Z), and **(d)** Perpendicular (X-Y) planes in the post heat treatment condition, relative to the vertical build direction.

allel (Y-Z) and perpendicular (X-Y) planes, relative to the primary vertical build direction. The inverse pole figures (IPF) in Fig. 15(a) and (b) represent the as-built condition and a high degree of tex-ture is exhibited in the build direction of the structure produced via LPBF. For comparison, the IPF figures in Fig. 15 (a) and (b) relate directly to the specimen and orientations illustrated in Fig. 6 (a)

and (b); the low-energy, as-built condition. Whilst the locations cannot be considered identical, the similarity of the grain boundaries present in the IPF maps compared to those in the micrographs in Fig. 6, is an indication that relative areas have been selected remote from the influence of the included simulated cooling holes. The grain structure in this orientation (Fig. 15(a)) exhibits a columnar type appearance, which has been reported here as well as elsewhere in the available literature [5,29,30]. Conversely, in the perpendicular plane in the as-built condition, a more equiaxed structure is observed with a greater spread in orientation, although the prevailing texture in the ⟨100⟩ direction is still evident, albeit to a lesser degree than in the parallel plane. A colony of grains is present in the centre of Fig. 15(b) that exhibit grain dimensions in X and Y that are much reduced compared to the mean grain size and, along with other isolated grains that can be seen around the IPF confirm the presence of grains that show the highest aspect ratio in Fig. 15(a).

IPF micrographs of the same structural features, produced using an identical set of build parameters, is shown in Fig. 15(c) and (d) after the application of the heat treatment described in Fig. 14. It can be seen in Fig. 15(c) that post heat treatment, the grain structure is equiaxed and has coarsened considerably with respect to the as-built condition. Visually, the high degree of texture has been diminished significantly from that shown in Fig. 15(a). The IPF for the parallel (X-Y) plane for the post heat treated Haynes 282 LPBF material is shown in Fig. 15(d) where the absence of small colonies and isolated smaller grains is notable as is the associated coarsening of the grain structure. Again, the removal of the texture and associated high aspect ratio grains present in the as-built condition is observed after heat treatment in Fig. 15(d). An additional artefact arising from the recrystallisation during heat treatment is the presence of annealing twins in the crystal structure of the additive Haynes 282, observed in Fig. 15(c) and (d), for the parallel and perpendicular planes respectively.

The change in texture of the samples can be seen in Fig. 16, between the as-built condition (Fig. 16(a)) and the heat treated condition (Fig. 16(b)) for the parallel plane only, considering all measured points using Channel 5 Mambo software. It is clearly apparent that the heavy ⟨100⟩ orientation present in the direction of grain growth is removed with a structure that exhibits little to no preferential orientation or texture. It is also evident that the strong texture present in Fig. 16(a) exhibits a definite rotation originating from the build process, which is approximately 67°. This rotation is consistent with the scanning strategy used here and reported elsewhere [31] for similar build parameters. The effects of this incremental epitaxial growth over each 30 μm layer is seen to have been vastly diminished post heat treatment.

Grain size measurements were also taken from the acquired EBSD data in the planes considered, i.e. parallel and perpendicular to the build direction. An elliptical fitting method was selected from the in-built functions in the Channel 5 Tango software package. In the analysis, any fitted grain with an effective diameter of<3 μm is not considered. The mean diameter of the grains in the as-built material in the perpendicular (X-Y) plane was determined by EBSD to be 12 μm, which is significantly lower than that observed under optical inspection (Table 7 and Fig. 6) however, this result may in part be influenced by the presence of the colony of smaller grains identified in Fig. 15(b). The aspect ratio determined in this plane was 2.3, whereas in the parallel (Y-Z) plane a corresponding aspect ratio of 6.2 and mean grain diameter of 29.2 μm was measured, indicating a high degree of anisotropy. The effect of the heat treatment applied was reflected in higher grain sizes determined in both parallel and perpendicular planes. Mean grain diameters of 44 μm and 63 μm were determined in the perpendicular (X-Y) and the parallel (Y-Z) planes respectively, where the latter can be seen to be in good agreement with optical observations (Table 8), with a corresponding maximum grain diameter of 330 μm being determined in the area considered by EBSD analysis.

Local misorientation data from the EBSD maps in the parallel (Y-Z) plane is given in the as-built and post heat treated conditions in Fig. 17(a) and (b) respectively. Local misorientation within the as-built sample is observed within the majority of the grains present, orientated in the direction of epitaxial grain growth. Post heat treatment, the overall misorientation present is seen to be significantly reduced (Fig. 17(b)).
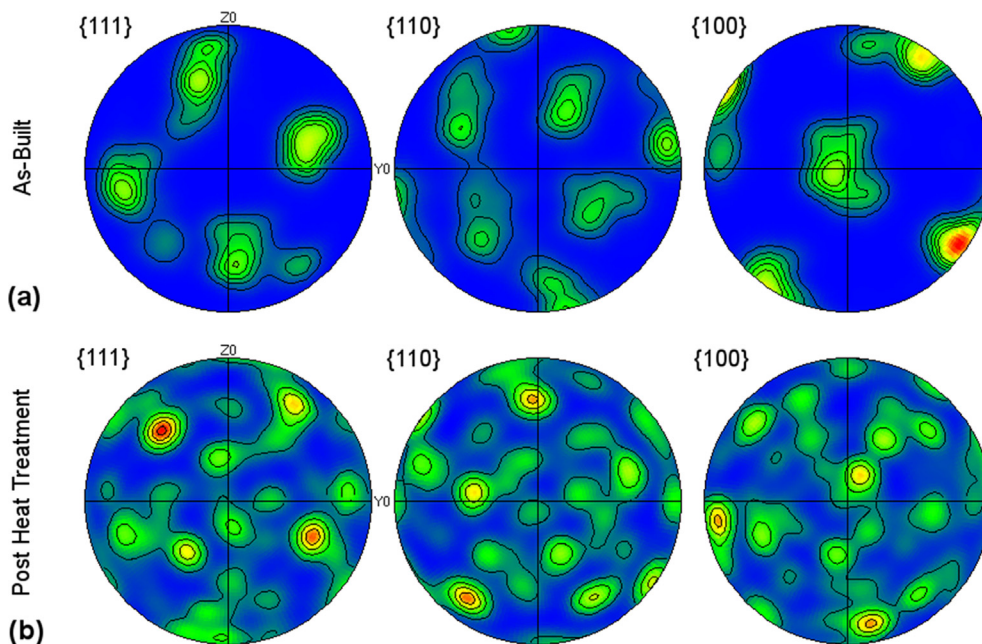

Fig. 16. Pole figure plots from EBSD data taken in the parallel (Y-Z) plane of LPBF Haynes 282 in **(a)** As-built condition, and **(b)** Post heat treatment condition.
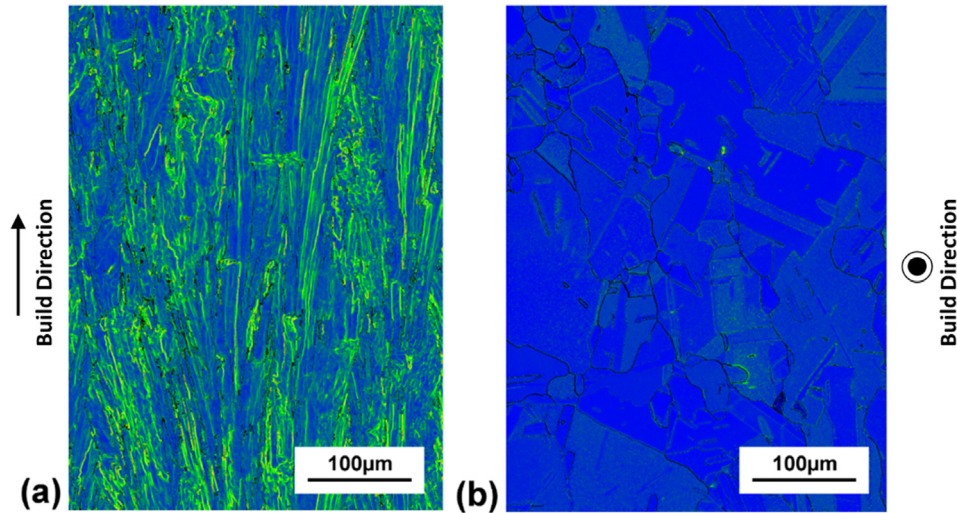
Fig. 17. Local misorientation plots from EBSD data taken in the parallel (Y-Z) plane to the vertical build direction in **(a)** As-built condition, and **(b)** Post heat treatment condition.

3.6. Mechanical testing

3.6.1. Vickers micro-hardness testing

The results from the hardness testing highlight the relative levels of anisotropy in the as-built material, as displayed in Fig. 18, and how this has been alleviated with the post build heat treatment. The hardness values for the as-built samples show a difference dependant on orientation relative to the build direction but also due to the variation in energy density for the three alternative parameter sets. In the as-built condition, hardness can be directly related to differences in grain size associated with changes in energy density, as given in Fig. 6 and Table 7. On the parallel Y-Z plane, the Vickers hardness value increases with higher energy densities and decreases in a more significant manner for samples

tested in the perpendicular X-Y orientation. This can be associated to the smaller average grain size (24.4 μm) and higher density of grain boundaries in the high energy density specimen leading to an increase in hardness (327.22 HV) in the parallel orientation, whereas the grain size in the lower energy density equivalent increases to 31.7 μm and the average hardness value drops to 312.17 HV. This behaviour in the as-built material is in accordance with Hall-Petch theory, and a similar trend is observed for the perpendicular X-Y plane, where an increase in the energy density leads to an increase in grain size (20.6 μm – 24.6 μm), and as consequence, a drop in hardness (326.72 HV-297.32 HV).

In the post heat treatment condition there are only small differences in Vickers hardness for the alternative energy densities and the different orientations relative to the vertical build orientation
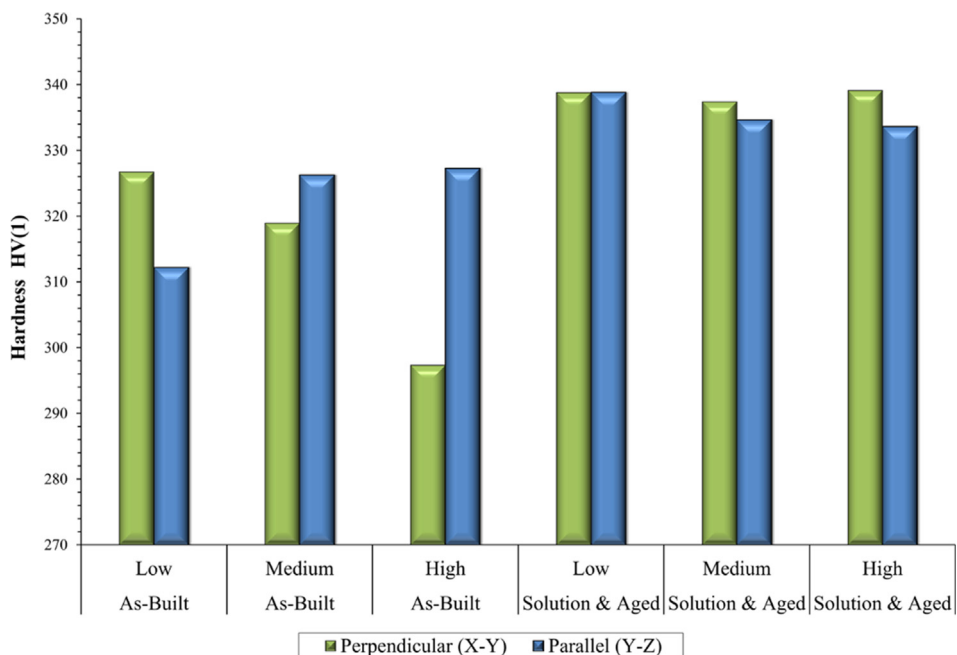

Fig. 18. Vickers hardness measurements for low, medium and high energy density builds for both as-built and post solution heat treated LPBF Haynes 282 in orientations parallel (Y-Z plane) and perpendicular (X-Y plane) to the vertical build direction.
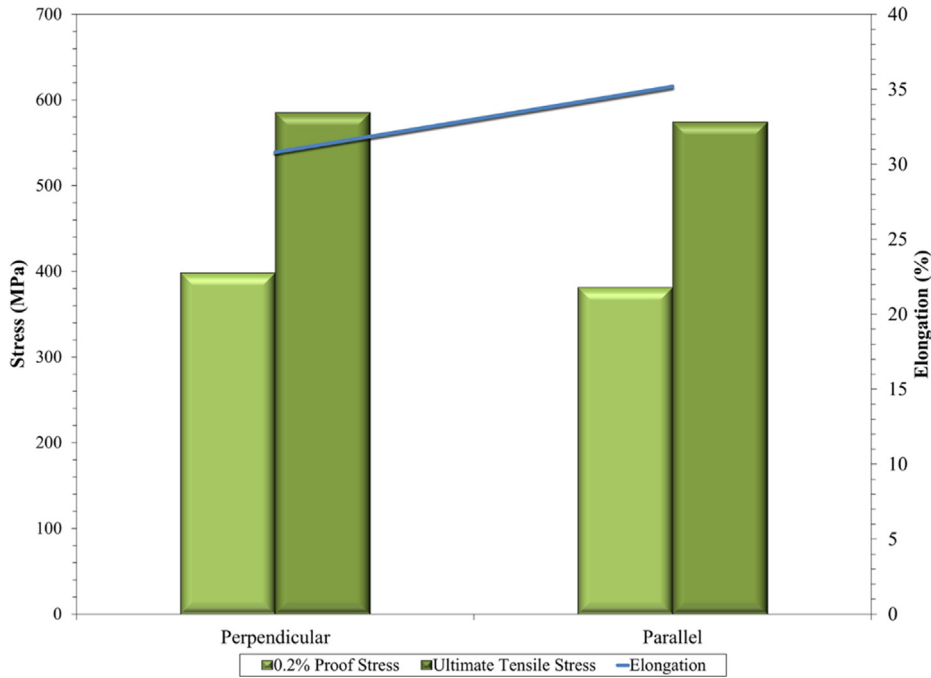
Fig. 19. Tensile properties for orientations perpendicular (X-Y plane) and parallel (Y-Z plane) to the vertical build direction in post solution heat treated LPBF Haynes 282 at 850 °C.

(Fig. 18). Overall the hardness values have increased relative to the as-built material, which is likely to be a result of a finer, more optimised distribution of γ' following the ageing heat treatment. The more homogeneous behaviour as a function of energy density is attributed to the anisotropy associated with the as-built material being replaced by a more equiaxed structure resulting from recrystallisation during the solution heat treatment, and the increased presence of twinning. The results emphasise the importance of selecting the correct solution heat treatment temperature to promote complete recrystallisation of the microstructure. The results also indicate that heat treatment has a greater importance than build parameters in determining the final properties of the alloy. In wrought alloys, the solution heat treatment temperature is generally selected to balance the requirement to dissolve the main strengthening γ' phase and prevent excessive grain growth [15]. However, in contrast, for LPBF materials the requirement is to reform the as-built microstructure to produce more isotropic material properties.

3.6.2. Tensile testing

The more isotropic mechanical behaviour found in the post solution heat treated material, as indicated by the hardness tests, is further supported by tensile tests at 850 °C on round cylindrical specimens extracted from both the parallel (Y-Z) and perpendicular (X-Y) planes to the vertical build direction. This can be seen in relation to the 0.2% proof stress and ultimate tensile strength values displayed in Fig. 19, where the samples taken perpendicular to the primary build orientation offer a marginally superior tensile performance, although the difference across the two alternative orientations would be considered to lie within the natural variation of tensile data. A marginal increase is again observed in elongation values as the parallel orientation is seen to exhibit a slightly more ductile response. This may be a remnant of the build orientation, however this variation is small in the context of the overall values of elongation which encouragingly exceed 30% in both the parallel and perpendicular orientated materials.
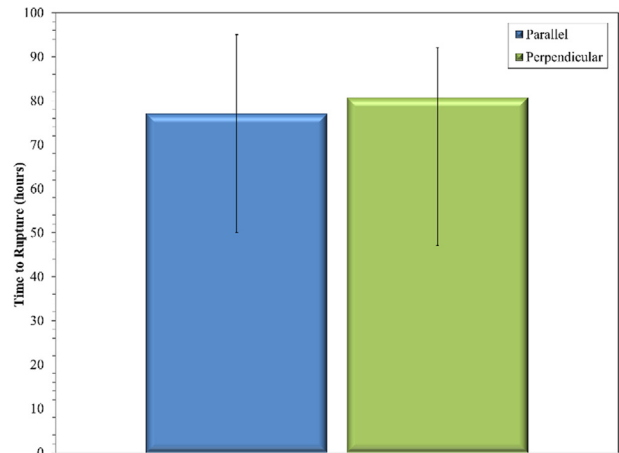

Fig. 20. Stress rupture properties for orientations parallel (Y-Z plane) and perpendicular (X-Y plane) to the vertical build direction in post solution heat treated LPBF Haynes 282.

3.6.3. Stress rupture testing

Comparing the stress rupture properties both parallel and perpendicular to the vertical build orientation in the post solution heat treatment condition shows there is very little difference between the stress rupture lives of the two data sets and it is likely that the test results form part of the same sample population (Fig. 20). For ductility, there is again a small difference between the contrasting orientations with the samples taken from the parallel Y-Z plane generally exhibiting greater ductility (20% compared to 16%), similar to the results found from the tensile testing. This again may be a remnant of the alignment of microstructure with the build direction. The average stress rupture life for the parallel and perpendicular specimens is found to be highly comparable with similar scatter between tests also apparent

Table 9
Analysis of Variance.

Source	Degrees of Freedom	Sum of Squares (SS)	Mean Squares (MS)	F-Value	P-Value
Energy Density (J/mm^2)	2	5130	2564.78	26.61	0.000
Error	40	3855	96.37		
Total	42	8984			

Table 10
Mean grain size (X-Y plane).

Energy Density (J/mm^2)	N	Mean (µm)	StDev (µm)	95% CI (µm)
Low	15	46.08	7.25	(40.96, 51.21)
Medium	14	62.21	11.67	(56.91, 67.51)
High	14	72.41	10.19	(67.11, 77.71)

Table 11
Tukey Pairwise Comparisons: Grouping Using the Tukey Method and 95% Confidence.

Energy Density (J/mm^2)	N	Mean	Grouping		
Low	15	46.08			C
Medium	14	62.21		B	
High	14	72.41	A		

Means that do not share a letter are significantly different.

Table 12
Student *T*-test results.

T-Test	$\sigma_{PS0.1\%}$ (MPa)	$\sigma_{PS0.2\%}$ (MPa)	σ_{UTS} (MPa)	Tensile Elongation (%)	Stress Rupture (h)	Stress Rupture Elongation(%)
X_v	391	381	574	35.2	77.05	20.33
X_h	409	398	585	30.8	80.69	16
S_v	7.42	7.42	5.48	3.03	18.26	4.59
S_h	15.17	16.05	9.35	1.30	17.50	3.16
n	5	5	5	5	6	6
$S/\sqrt{n}$	6.78	7.18	4.18	0.58	7.14	1.29
$(Xv-Xh)$	18	17	11	4.40	3.64	4.33
T	2.65	2.37	2.63	7.55	0.51	3.36
DF (n-1)	4	4	4	4	5	5
$\alpha/2$	0.025	0.025	0.025	0.025	0.025	0.025
$T_{.975}$	2.78	2.78	2.78	2.78	2.57	2.57
H_0 (95%)	Accept	Accept	Accept	Reject	Accept	Reject

in each data set. Therefore, the overall conclusion is that stress rupture life is not influenced by the orientation of the samples relative to the vertical build direction following the solution and aging heat treatment.

3.7. Statistical analysis

3.7.1. Grain size post heat treatment

Grain size is inherently important because of its effect on both tensile, through Hall-Petch effects [32], and creep properties due to grain boundary sliding [33]. Therefore, it is of interest to determine the effects of melt parameters on the resulting microstructure. The Minitab^{TM} statistical analysis software has been used to analyse grain structure measurement data. A summary of the results of the Minitab^{TM} analysis is presented in Tables 9, 10 and 11. The results indicate that the mean values for each Energy Density level are significantly different, based on a 95% confidence interval. The importance of this result is that even after heat treatment, which has significantly normalised the microstructure, build parameters can still affect the final microstructure.

The critical F-ratio for α = 0.05 is 3.24 based on a sample size of 14. The F-Value in Table 10 is much greater than the critical value, therefore the result has a high level of significance indicated by the

P-Value $\ll$ 0.05. Table 10 shows the mean ranges for the 95% confidence intervals. Table 11 shows the grouping of the different Energy Density levels. Each level has a different grouping indicating that the means for each level are significantly different.

3.7.2. Mechanical properties

The results of the *T*-test comparison between the as-built samples taken both parallel and perpendicular to the vertical build direction are summarised in Table 12. The results indicate that at 850 °C, 0.1% proof stress ($\sigma_{PS0.1\%}$), 0.2% proof stress ($\sigma_{PS0.2\%}$), and ultimate tensile strength (σ_{UTS}) values for both parallel (Y-Z) and perpendicular (X-Y) specimens have the same mean properties, i.e. the Null hypothesis is accepted. For tensile elongation however, the null hypothesis is rejected. Therefore, for a 95% confidence interval, parallel and perpendicular test specimens do not have the same mean values since the specimens built parallel to the build direction exhibit greater mean tensile elongation than those built in the perpendicular orientation.

For stress rupture tests at 750 °C, similar results are observed; mean stress rupture lives have the same population means based on the null hypothesis test, whilst the mean creep ductility, in terms of elongation, is greater for the samples built parallel to the vertical build orientation as the null hypothesis is rejected.

4. Conclusions

In this study, an in-depth analysis was conducted to determine the influence of build orientation and post process treatments on the microstructure and mechanical properties of the Ni based superalloy Haynes 282. Advanced microscopy methods and different mechanical test approaches have been utilised and the following conclusions have been drawn:

- The as-built grain size has been found to be directly influenced by build parameters where higher energy density builds produced grains that appear larger in the plane perpendicular to the build direction (X-Y plane), but shorter in height yet wider grains in the orthogonal parallel Y-Z plane.
- Post solution heat treatment and aging was found to promote grain growth and recrystallisation, resulting in a bi-modal grain structure with both large (563 μm diameter) and small (2 μm diameter) grains co-existing in the same structure. The average grain size in the post solution heat treated and aged condition was found to still be influenced by the input build parameters. The smallest average grain size in the post build condition (44 μm) was measured from the lowest energy density build and the largest average grain size (69 μm) was recorded in the highest energy density build.
- EBSD mapping confirmed that the solution heat treatment was effective in alleviating the strongly textured grain morphology observed in the as-built material, and the overall misorientation is seen to be reduced.
- The variation in average grain size associated with changing energy density has been found to have an influence on the mechanical properties of the as-built material. The microhardness results are controlled by the input energy density and the subsequent resulting grain size, which is found to directly control hardness properties through a Hall-Petch relationship.
- The grain size in the post solution heat treated and aged condition is more isotropic and there is much less variation in microhardness as reflected by the high level of consistency in the results, despite the deviation in input energy density. However, the γ' precipitate morphology was dendritic and appeared overaged, but still provided an overall increase in the hardness values. Further investigation showed that the cooling rate (approximately $4\,°C.min^{-1}$) fell below the target cooling regime specified for post LPBF solution heat treatment.
- Tensile tests at 850 °C in the post solution and age heat treated material demonstrated that both the average σ_{UTS} and $\sigma_{PS0.2\%}$ values are highly comparable across the two contrasting orientations, whilst ductility, in terms of percentage elongation, is greater in the parallel plane.
- Stress rupture creep lives at 750 °C in the post solution and age heat treatment condition were not found to be affected by build orientation, however a reduction in ductility was observed in the perpendicular samples, similar to the tensile data.

Declaration of Competing Interest

The authors declare that they have no known competing financial interests or personal relationships that could have appeared to influence the work reported in this paper.

Acknowledgments

References

[1] W.E. Frazier, Metal Additive Manufacturing: A Review, J. Mater. Eng. Perform. 23 (6) (2014) 1917–1928.

[2] T. Debroy, H. Wei, J. Zuback, T. Mukherjee, J. Elmer, J.O. Milewski, A. Beese, A. Wilson-Heid, A. De, W. Zhang, Additive manufacturing of metallic components – Process, structure and properties, Prog. Mater Sci. 92 (2018) 112–224.

[3] M. Thomas, G.J. Baxter, I. Todd, Normalised model-based processing diagrams for additive layer manufacture of engineering alloys, Acta Mater. 108 (2016) 26–35.

[4] B. Song, X. Zhao, S. Li, C. Han, Q. Wei, S. Wen, J. Liu, Y. Shi, Differences in microstructure and properties between selective laser melting and traditional manufacturing for fabrication of metal parts: A review, Frontiers of Mechanical Engineering 10 (2015) 111–125.

[5] G.P. Dinda, A.K. Dasgupta, J. Mazumder, Texture control during laser deposition of nickel-based superalloy, Scr. Mater. 67 (5) (2012) 503–506.

[6] S.B. David, S.S. Babu, J.M. Vitek, Weldability and Microstructure Development in Nickel-Base Superalloys, Numerical Analysis of Weldability, Graz, Austria, 1997.

[7] Y.L. Wang, O.A. Ojo, R.G. Ding, M.C. Chaturvedi, Weld metal cracking in laser beam welded single crystal nickel base superalloys, Mater. Sci. Technol. 25 (1) (2009) 68–75.

[8] L.O. Osoba, A.K. Khan, S.O. Adeosun, Cracking susceptibility after post-weld heat treatment in Haynes 282 nickel based superalloy, Acta Metallurgica Sinica (English Letters) 26 (6) (2013) 747–753.

[9] A.S. Shaikh, F. Schulz, K. Minet-Lallemand, E. Hryha, Microstructure and mechanical properties of Haynes 282 superalloy prodcued by laser powder bed fusion, Mater. Today Commun. 26 (2021) 102038.

[10] E. Chlebus, B. Kuźnicka, T. Kurzynowski, B. Dybała, Microstructure and mechanical behaviour of Ti–6Al–7Nb alloy produced by selective laser melting, Mater. Charact. 62 (5) (2011) 488–495.

[11] L.N. Carter, X. Wang, N. Read, R. Khan, M. Aristizabal, K. Essa, M.M. Attallah, Process optimisation of selective laser melting using energy density model for nickel based superalloys, Mater. Sci. Technol. 32 (7) (2016) 657–661.

[12] J. Risse, LM Productivity Improvement, in Development of Aero Engine Component Manufacturing using Laser Additive Manufacturing, European Commission, Fraunhofer ILT, Aachen, Germany, 2014, 12-16.

[13] V.D. Divya, R. Muñoz-Moreno, O.M.D.M. Messé, J.S. Barnard, S. Baker, T. Illston, H.J. Stone, Microstructure of selective laser melted CM247LC nickel-based superalloy and its evolution through heat treatment, Mater. Charact. 114 (2016) 62–74.

[14] R. Muñoz-Moreno, V.D. Divya, S.L. Driver, O.M.D.M. Messé, T. Illston, S. Baker, M.A. Carpenter, H.J. Stone, Effect of heat treatment on the microstructure, texture and elastic anisotropy of the nickel-based superalloy CM247LC processed by selective laser melting, Mater. Sci. Eng., A 674 (2016) 529–539.

[15] C. Joseph, C. Persson, M. Hörnqvist Colliander, Influence of heat treatment on the microstructure and tensile properties of Ni-base superalloy Haynes 282, Mater. Sci. Eng., A 679 (2017) 520–530.

[16] ASTM International: West Conshohocken, Standard Test Methods for Determining Average Grain Size, West Conshohocken, PA, 2013.

[17] ASTM International: West Conshohocken, ASTM E21-17e1 Standard Test Methods for Elevated Temperature Tension Tests of Metallic Materials, 2017.

[18] ASTM International: West Conshohocken, ASTM E139-11 Standard Test Methods for Conducting Creep, Creep-Rupture, and Stress-Rupture Tests of Metallic Materials, 2011.

[19] K.S. Krishnamoorthi, V.R. Krishnamoorthi, A First Course in Quality Engineering: Integrating Statistical and Management Methods of Quality, Second Edition., Taylor & Francis, 2011.

[20] J.L. Caron, Weldability and Welding Metallurgy of Haynes 282 Alloy, 8th International Symposium on Superalloy 718 and Derivatives, John Wiley & Sons (2014), 273-286.

[21] D.A. Metzler, A gleeble based method for ranking the Strain Age Cracking susceptibiliy of Ni-based Superalloys, Welding Journal 87 (2008) 249–256.

[22] N.J. Harrison, I. Todd, K. Mumtaz, Reduction of micro-cracking in nickel superalloys processed by Selective Laser Melting: A fundamental alloy design approach, Acta Mater. 94 (2015) 59–68.

[23] J.P. White, N. Read, R.M. Ward, R. Mellor, M. Attallah, Prediction of melt pool profiles for selective laser melting of AlSi10Mg alloy, Materials Science and Technology Conference and Exhibition 2014 (2014) 1985–1992.

[24] D. Deng, R.L. Peng, H. Brodin, J. Moverare, Microstructure and mechanical properties of Inconel 718 produced by selective laser melting: Sample orientation dependence and effects of post heat treatments, Mater. Sci. Eng., A 713 (2018) 294–306.

[25] D. Tomus, T. Jarvis, X. Wu, J. Mei, P. Rometsch, E. Herny, J.F. Rideau, S. Vaillant, Controlling the Microstructure of Hastelloy-X Components Manufactured by Selective Laser Melting, Physics Procedia 41 (2013) 823–827.

[26] F.B. Royer, Y, Study of the departure from equilibrium and of the thermal behavior of Ni-based superalloy powders and dense materials manufactured by selective laser melting, Armines (2014) 1–10.

[27] M.J. Cieslak, T.J. Headley, G.A. Knorovsky, A.D. Romig, T. Kollie, A comparison of the solidification behavior of INCOLOY 909 and INCONEL 718, Metall. Trans. A 21 (1) (1990) 479–488.

[28] L.O. Osoba, R.G. Ding, O.A. Ojo, Improved resistance to laser weld heat-affected zone microfissuring in a newly developed superalloy HAYNES 282, Cracking susceptibility after post-weld heat treatment in Haynes 282 nickel based superalloy, Metallurgical and Materials Transactions A 43 (2012) 4281–4295.

[29] A. Ramakrishnan, G.P. Dinda, Functionally graded metal matrix composite of Haynes 282 and SiC fabricated by laser metal deposition, Mater. Des. 179 (2019) 107877.

[30] G.P. Dinda, A.K. Dasgupta, J. Mazumder, Evolution of microstructure in laser deposited Al–11.28%Si alloy, Surf. Coat. Technol. 206 (8) (2012) 2152–2160.

[31] F. Geiger, K. Kunze, T. Etter, Tailoring the texture of IN738LC processed by selective laser melting (SLM) by specific scanning strategies, Mater. Sci. Eng., A 661 (2016) 240–246.

[32] R.W. Armstrong, Comparison of grain size and strain rate influences on higher temperature metal strength and fracturing properties, Strength Fract. Complexity 11 (2018) 121–135.

[33] P.N. Quested, S. Osgerby, Mechanical properties of conventionally cast, directionally solidified, and single-crystal superalloys, Mater. Sci. Technol. 2 (5) (1986) 461–475.